

# Crystal growth and magnetic behavior of $J_{\text{eff}} = 1/2$ quantum antiferromagnet $\text{CeCl}_3$

Nashra Pistawala<sup>1</sup>, Luminata Harnagea<sup>1</sup>, Suman Karmakar<sup>2</sup>, Rajeev Rawat<sup>2</sup>, and Surjeet Singh<sup>1\*</sup>

<sup>1</sup>Department of Physics, Indian Institute of Science Education and Research, Pune 411008

<sup>2</sup>UGC-DAE Consortium for Scientific Research, University Campus, Khandwa Road, Indore 452 001

\* surjeet.singh@iiserpune.ac.in

## Abstract

We have grown high-quality single crystals of  $\text{CeCl}_3$  using a modified Bridgman Stockbarger method in an infrared image furnace. These crystals are characterized using single-crystal x-ray diffraction, Laue x-ray diffraction, Raman spectroscopy, magnetization, and heat capacity probes.  $\text{CeCl}_3$  crystallizes with a trigonal crystal structure (space group P-3, # 147). The magnetic susceptibility shows a broad peak centered around 50 K. The crystal field split  $J = 5/2$  manifold of  $\text{Ce}^{3+}$  in  $\text{CeCl}_3$  has an effective spin  $1/2$ ,  $|5/2, \pm 5/2\rangle$  Kramer's doublet ground. The exchange coupling between the Ce moments is rather weak (Weiss temperature  $\sim 0.2$  K). The magnetic specific heat or  $C_{4f}$  shows a Schottky anomaly around 30 K due to the excited crystal field doublets located near 55 K and 155 K. The Raman spectra at 300 K exhibits five clearly resolvable modes at  $106.8 \text{ cm}^{-1}$ ,  $181.2 \text{ cm}^{-1}$ ,  $189 \text{ cm}^{-1}$ ,  $213 \text{ cm}^{-1}$ , and  $219.7 \text{ cm}^{-1}$ .

## 1 Introduction

Quantum antiferromagnets have garnered enormous attention in the past few years. They exhibit exotic phases at low temperatures, including, the much-celebrated Quantum Spin Liquids (QSLs) state characterized by fractional excitations and long-range entanglement [1]. The triangular and Kagome lattice antiferromagnets are ideal platforms to realize a QSL phase. In 2009, Kitaev proposed an exactly solvable model for anisotropic spin  $1/2$  on a honeycomb lattice, the ground state of which is an exotic QSL with Majorana fermions as excitations. Unlike geometric frustration, where the frustration arises due to the geometry of the underlying lattice, in the Kitaev model it is the bond-dependent Ising like interactions that gives rise to a strong frustration. The iridates (e.g.,  $\text{Na}_2\text{IrO}_3$ ) and the ruthenates (e.g.,  $\text{RuCl}_3$ ) have been extensively studied to realize the Kitaev model and search for half-quantization plateau in thermal Hall effect which would confirm the existence of Majoranas [2,3]. Recently,  $\text{YbCl}_3$ , a rare-earth trichloride, has also attracted

attention as a quantum antiferromagnet with a honeycomb lattice of the  $\text{Yb}^{3+}$  ions in a Kramer's doublet ground state ( $J_{\text{eff}} = 1/2$ ) [4].  $\text{YbCl}_3$  belongs to the rare-earth trichloride family with general formula  $\text{RCl}_3$  ( $\text{R}$  = Rare earth element). While the heavier rare-earth members ( $\text{R} = \text{Tb}$  to  $\text{Lu}$ ) of this series crystallize with a monoclinic structure where the  $\text{R}^{3+}$  ions form a honeycomb lattice, the lighter members ( $\text{R} = \text{La}$  to  $\text{Gd}$ ) crystallize with a hexagonal structure where the  $\text{R}^{3+}$  ions are arranged on triangular plaquettes stacked to form chains of  $\text{R}^{3+}$  ions running parallel to the  $c$ -axis [5–7]. Here, we focus on the member  $\text{CeCl}_3$  of this series which is an antiferromagnetic insulator with an electronic band gap of 4.3 eV [8]. Both  $\text{Yb}^{3+}$  and  $\text{Ce}^{3+}$  are Kramer's ions but while  $\text{Yb}^{3+}$  is just one short of a completely filled  $f$ -shell,  $\text{Ce}^{3+}$  has only one electron in the  $f$ -shell. The previous reports on  $\text{CeCl}_3$  concentrated only on the low-temperature behavior of  $\text{Ce}^{3+}$  moments in the temperature range from 0.1 K to 4.2 K, and in magnetic fields up to 12 kOe using the magnetic susceptibility and specific heat probes [9]. The Cl Nuclear Quadrupole Resonance (NQR) on some rare-earth trichlorides and tribromides has also been reported previously over the same temperature range [10]. According to these reports, in  $\text{CeCl}_3$ ,  $\text{Ce}^{3+}$  ions carry an effective spin 1/2, which undergo long-range antiferromagnetic ordering around 0.11 K. The physical properties of these compounds show strong sample dependence, which has been attributed to the presence of impurities in the sample [9]. To clarify the exact ground state of these interesting quantum antiferromagnets mandates the availability of high-quality single crystals. Recently,  $\text{CeCl}_3$  gained considerable attention as a recent study argues that the optically driven chiral phonon modes in  $\text{CeCl}_3$  should generate giant effective magnetic fields ( $\sim 10^2$  T) acting on the paramagnetic  $4f$  spins [11]. This requires high-quality crystals where the induced magnetization can be probed experimentally via the inverse Faraday effect.

Here, we report the crystal growth, structural and physical characterizations of high-quality single crystals of  $\text{CeCl}_3$ . The mm-size, transparent, high-quality crystals are grown by the modified Bridgman-Stockbarger method using an infrared image furnace. The grown crystals are characterized using powder and single-crystal x-ray diffraction, and Laue diffraction. The magnetic susceptibility and specific heat are measured from liquid Helium temperature to near room temperature. The susceptibility shows a broad peak centered at 50 K. The Ce ions carry an effective spin 1/2 with Kramer's doublet  $|5/2, \pm 5/2\rangle$  ground state. The Ce-Ce exchange coupling is weak ( $\sim 0.2$  K). The specific heat shows an upturn upon cooling below 4 K, but no peak due to long-range ordering could

be seen down to a temperature of 2 K in zero-field measurement. Under an applied field, the low-temperature specific heat changes substantially with a peak appearing at 2.5 K under a field of 3 T. The zero-field magnetic specific heat above 2 K shows a Schottky anomaly around 30 K due to the excited crystal doublets of  $J = 5/2$  manifold. The best fit suggests the position of excited Kramer's doublets to be near 55 and 155 K.

## 2 Experimental Methods

Single crystals of anhydrous  $\text{CeCl}_3$  are grown from a stoichiometric melt using the two different methods: the static Bridgman method and traditional Bridgman-Stockbarger method in an image furnace. The details of the crystal growth methods and experiments are given in Sec. III.A. Single crystal X-ray diffraction was carried out using a Bruker Smart Apex Duo diffractometer at 100 K using Mo  $K\alpha$  radiation ( $\lambda = 0.71073 \text{ \AA}$ ). The total exposure time was 2.01 h. The frames were integrated using the Bruker SAINT software package [24] using a narrow frame algorithm. Data were corrected for absorption effects using the multiscan method (SADABS) [25]. The structure has been solved and refined using the Bruker SHELXTL software package. The grown crystals were oriented using a Laue camera (Photonic Science, UK) in backscattering geometry using Tungsten as a source material ( $\lambda = 0.35 \text{ \AA} - 2.5 \text{ \AA}$ , accelerating voltage 30 kV, Tube current 0.3 mA). The Laue pattern was analyzed using Orient Express 3.4 (V 3.3) software package. Raman spectra were collected at room temperature in backscattering configuration using a Horiba Jobin-Yvon LabRAM HR spectrometer equipped with liquid nitrogen cooled Charge-Coupled Detector (CCD) and laser of 532 nm as a source of excitation. The excitation was maintained at 25% of the maximum power, and the accumulation time for each spectrum was 30 s with 25 iterations each time to get better resolution and intensity of the Raman modes. The  $\text{CeCl}_3$  crystal was coated with a thin layer of Apizon N grease to prevent degradation due to its extremely hygroscopic nature. The Raman signal from the Apizon N was measured separately and subtracted from the total signal to eliminate the background. The Specific-heat measurements were done using the relaxation method in a Physical Property Measurement System (PPMS), Quantum Design, USA. A small piece of crystal, weighing around 10 mg, was cut into a 2 mm by 2 mm piece and mounted on the heat capacity sample holder using a low-temperature Apizon N grease. The addenda (heat capacity of sample holder and Apizon N grease) was measured before loading the sample. Sample degradation from moisture effect is minimized by handling, weighing and cutting

of  $\text{CeCl}_3$  crystal inside the glove box. The magnetic susceptibility was measured at the UGC-DAE center, Indore, using a VSM probe option in a Physics Property Measurement System (PPMS), Quantum design, USA. A single-crystal, approximately 4.1 mg, was mounted on a brass sample holder using the non-magnetic GE Varnish

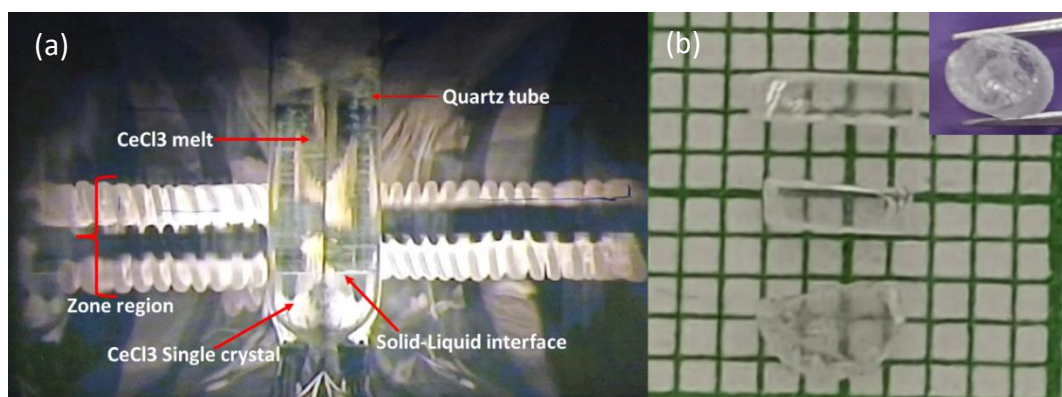


**Fig. 1.** (a) Crystal growth of  $\text{CeCl}_3$  using a four-mirror image furnace equipped with 1 kW halogen lamps. The lower part below the solid-liquid interface is the  $\text{CeCl}_3$  crystal being grown. (b) Images of the crystals pieces obtained after cutting the crystal boule shown in the inset.

### 3 Results and Discussion

#### 3.1 Crystal growth

The crystals of rare-earth trichlorides can be grown using the chemical vapor transport method employing  $\text{AlCl}_3$  as the transporting agent [12]. In this reaction, the rare-earth (R) oxides are first reacted with  $\text{AlCl}_3$  to form corresponding anhydrous rare-earth trichlorides. These are then further reacted with an excess  $\text{AlCl}_3$  through a reversible reaction to form gaseous complexes, including  $\text{RAl}_3\text{Cl}_{12}$  and  $\text{RAl}_4\text{Cl}_{15}$ . These gaseous complexes, having a significantly high vapor pressure, are transported to the colder end of the tube, where mm-sized transparent crystals of  $\text{RCl}_3$  can be extracted. This method is however complex and the resulting crystals are small and not of very high quality. Mroczkowski et al. reported crystal growth of  $\text{EuCl}_3$  using the vertical Bridgman method in the presence of  $\text{Cl}_2$  gas under high pressure [13]. The anhydrous rare-earth trichlorides  $\text{RCl}_3$  in general and  $\text{CeCl}_3$  in particular are highly sensitive to moisture and react readily to form  $\text{RCl}_3 \cdot x\text{H}_2\text{O}$  upon coming in contact with the ambient air. This reaction happens over a time scale of few minutes. It is therefore difficult to grow large, transparent single crystals of rare-earth trichlorides from a melt as the adsorbed moisture, when not carefully removed, reacts with

$\text{RCl}_3$  at elevated temperatures leading to a formation of various oxychlorides (e.g.,  $\text{ROCl}$ ) which makes the melt hazy. The grown crystal in such cases also has a hazy appearance with large number of cracks. It is, therefore, necessary to remove the absorbed moisture either by dehydration under a dynamic vacuum at slow rate or by chlorination of the melt using a mixture of ultra-pure argon gas and  $\text{CCl}_4$  [14]. A similar method has been described for the crystal growth of  $\text{CeCl}_3$  in Ref. [9].

In this work, high-quality single crystals of anhydrous  $\text{CeCl}_3$  are grown from a stoichiometric melt using two different methods: the static Bridgman method and traditional Bridgman-Stockbarger method in an image furnace. The anhydrous  $\text{CeCl}_3$  powder (Alfa Aesar 99.9%) was stored and handled in an argon filled glove box where  $\text{O}_2$  and  $\text{H}_2\text{O}$  level is maintained at less than 0.1 ppm at all times. The as-purchased powder, though labeled anhydrous, is not suitable for the crystal growth due to the presence of absorbed moisture which should be carefully removed first. We therefore first heat-treat the  $\text{CeCl}_3$  powder under dynamic vacuum. The powder is loaded in a dehydrated quartz ampoule. The ampoule was dehydrated by heating overnight at  $1000^\circ\text{C}$ . The loaded ampoule was removed from the glove box and connected to a turbomolecular pump. The other end of the ampoule (where the  $\text{CeCl}_3$  powder is located) was then introduced into a furnace whose temperature was gradually raised to  $230^\circ\text{C}$ . After heating at this temperature for 24 h under dynamic vacuum, the ampoule was allowed to cool down to room temperature and flame-sealed under dynamic vacuum ( $\sim 10^{-5}$  mbar). Up to here the procedure is common for both the methods.

*Static Bridgman:* In the case of static Bridgman method, the sealed ampoule was placed in a vertical tubular furnace with a temperature gradient. The furnace was heated to  $870^\circ\text{C}$ , which is higher than the melting point of anhydrous  $\text{CeCl}_3$  ( $817^\circ\text{C}$ ), at a rate of  $50^\circ\text{C/h}$  and allowed to dwell at this temperature for 12 h. After this, the furnace was slowly cooled to  $750^\circ\text{C}$  at a rate of  $0.3^\circ\text{C/h}$ , and finally cooled down to room temperature at a rate of  $50^\circ\text{C/h}$ . Shiny transparent crystals measuring up to a few mm in size were extracted from the ampoule.

*Bridgman-Stockbarger:* In this case, the size of the quartz ampoule taken is about 4-5 mm ID and 8 mm OD. In the first step, the ampoule is placed in a muffle furnace and heated up to  $850^\circ\text{C}$  to obtain a premelted, highly dense ingot about 15-20 mm long (the length of material in the tube shrinks by more than 50%) which is subjected to the crystal growth in

an infrared image furnace. For this the premelted ingot in the quartz ampoule was loaded in a four-mirror image furnace by suspending it from the upper shaft of the furnace (see, Fig. 1a). The shaft was lowered until the lower end of the ampoule reached the center of the furnace (the common foci of the ellipsoidal reflectors) where the light rays converge to form the molten-zone during the floating zone experiment [15]. The lamp power was then gradually increased to a value where  $\text{CeCl}_3$  started melting. After achieving a homogenous melt, the ampoule was allowed to travel downwards into the region of steep vertical temperature gradient. The lamps used were 1 KW each with the zone region of about 8-10 mm length. In a mirror furnace with 1 KW lamps, the vertical temperature gradient outside the molten zone is typically several hundred  $^{\circ}\text{C}/\text{cm}$ . In order to optimize the growth parameters to obtain crack-free high-quality crystals, several growth experiments were conducted at various traveling speeds, varying from  $1 \text{ mm h}^{-1}$  to  $0.2 \text{ mm h}^{-1}$ . At  $1 \text{ mm h}^{-1}$ , the crystal boule developed numerous cracks yielding very small, irregular shaped, crystal pieces. At slower growth speeds the results improved, but even at the slowest growth speed of  $0.2 \text{ mm h}^{-1}$  the cracks could not be avoided completely. In this case, however, the cracks were few and hence large (several mm by several mm across) crystal pieces could be obtained. The obtained crystal boule was cut using a low-speed saw inside the glove box. While cutting, small rectangular crystal pieces cleaved off the crystal boule. These crystal pieces are fully transparent with atomically flat facets as shown in Fig. 1(b). The flat surfaces of the semicircular piece were dry polished using a silicon-carbide paper of grit-size 1200. The slight haziness seen is due to imperfect surface polishing and not because the crystal piece is hazy inside.

Between the two growth methods, the crystals obtained using the image furnace are of higher quality. They are fully transparent and are free from defects. The presence of defects or impurities (typically oxychlorides mentioned above) in the crystal leads to hazy or milky appearance. The x-ray diffraction pattern, recorded in the Bragg-Brentano geometry on one of the crystal specimens, is shown in Fig. 2. The image of the specimen is shown as an inset. The pattern is collected from the flat surface of the specimen. The only reflections seen are those corresponding to the *bc*-plane. This shows that the specimen being investigated is an oriented single crystal of high-quality. The orientation of the surface was further confirmed using the x-ray Laue diffraction (see left inset in Fig. 2), where sharp Laue spots were observed, which suggest that the grown crystals are of high quality.

### 3.2 Single crystal X-ray diffraction

A small crystal was selected for single crystal x-ray diffraction (SCXRD). Table 1 gives the summary of crystallographic parameters. Table 2 summarizes the data collection and structure refinement parameters. The atomic coordinates and isotropic atomic displacement parameters are given in Table 3. As shown in Table 2, the values of the R-factors are satisfactory, and the value of goodness-of-fit parameter is close to 1, indicating a good agreement between the experimental data and the crystallographic model.

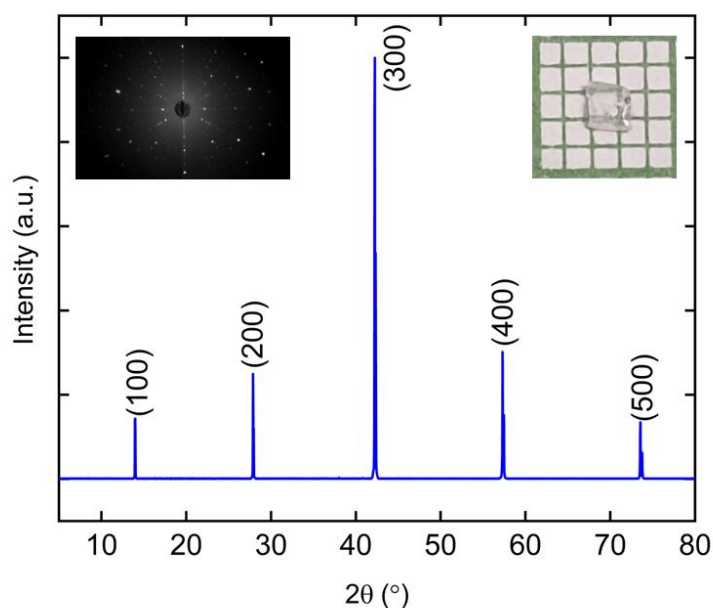


**Fig. 2.** (a) The x-ray diffraction pattern carried out in the Bragg-Brentano geometry on the specimen shown in the inset on the right. The left inset shows the Laue diffraction pattern from a similar specimen as shown here.

The schematic of the crystal structure of  $\text{CeCl}_3$  is shown in Fig. 3.  $\text{CeCl}_3$  crystallizes in a trigonal crystal structure with space group P-3 (No. 147). In this structure, each  $\text{Ce}^{3+}$  ion is nine-fold coordinated by  $\text{Cl}^-$  ions, as shown in Fig. 3(c). Of these, three  $\text{Cl}^-$  are coplanar with the central  $\text{Ce}^{3+}$  ion. These are labelled 1 to 3 in Fig. 3(c). The other six  $\text{Cl}^-$  ions are located above and below the central  $\text{Ce}^{3+}$  ion. These are labelled from 4, 5 and 6 (above), and 7, 8 and 9 (below) in Fig. 3(c). When viewed along the b-axis, the  $\text{Ce}^{3+}$  ions form a zig-zag chain running parallel to the c-axis as shown in Fig. 3(a). The Ce-ions marked with yellow border are the nearest neighbors each at a distance of 4.3126 Å from the central Ce ion (blue) along the c-axis. The three second-nearest neighbors, each at a distance of 4.7980 Å, are shown using magenta, and the third neighbors at a distance of 7.4230 Å are shown

using the red border (See Fig. 3(b)). The polyhedral around the  $\text{Ce}^{3+}$  are edge-sharing, forming a ring in the  $ab$ -plane as shown in Fig. 3(b). The exchange between any two nearest neighbor Ce ions is via three Ce–Cl–Ce pathways along the  $c$ -axis where the Ce–Cl–Ce bond angle is  $95.4^\circ$ , as shown in Fig. 3(d). The second-nearest neighbor interaction is mediated via two Ce–Cl–Ce pathways with bond angle Ce–Cl–Ce of  $110.4^\circ$ , as shown in Fig. 3(e). The crystal structure reported in the earlier publications is of slightly higher symmetry ( $P6_3/m$ , 176) [5–7] compared to the crystal structure in the present report ( $P-3$ , 147). A plausible reasons for this discrepancy could be that in all the earlier reports, the crystal structure determination was based on powder x-ray diffraction technique [5–7]. On the other hand, in the present work the data are collected on a high-quality single crystal specimen using a four-circle diffractometer at 100 K. The crystal structure data from different reports is summarized in the Table S1 in the Supplementary Material.

**Table 1 .** Summary of the crystallographic data

Chemical formula	$\text{CeCl}_3$
Formula weight	246.47 g/mol
Temperature	273(2) K
Wavelength	0.71073 Å
Crystal system	trigonal
Space group	$P-3$
Unit cell dimensions	$a = 7.4238(11)$ Å $\alpha = 90^\circ$ $b = 7.4238(11)$ Å $\beta = 90^\circ$ $c = 4.3126(9)$ Å $\gamma = 120^\circ$
Volume	$205.84(7)$ Å <sup>3</sup>
$Z$	2
Density (calculated)	$3.977$ g/cm <sup>3</sup>
Absorption coefficient	$12.762$ mm <sup>-1</sup>
$F(000)^*$	218

\*  $F(000)$  is structure factor calculated at  $h = k = l = 0$  and indicates the effective number of electrons in the unit cell



**Table 2.** Data collection and structure refinement for CeCl<sub>3</sub> single crystals.

Theta range for data collection	3.17 to 28.65°	
Index ranges	-10≤h≤9, -6≤k≤10, -5≤l≤5	
Reflections collected	2703	
Independent reflections	358 [R(int) = 0.0326]	
Coverage of independent reflections	100.0%	
Absorption correction	Multi-Scan	
Structure solution technique	direct methods	
Structure solution program	SHELXT 2014/5 (Sheldrick, 2014)	
Refinement method	Full-matrix least-squares on F <sup>2</sup> <sup>£</sup>	
Refinement program	SHELXL-2018/3 (Sheldrick, 2018)	
Function minimized	$\Sigma w(F_{oo}^2 - F_{cc}^2)^2$ <sup>£</sup>	
Data / restraints / parameters	358 / 0 / 14	
Goodness-of-fit on F <sup>2</sup>	1.189	
Final R indices	358 data; I>2σ(I)	R <sub>1</sub> = 0.0151, wR <sub>2</sub> = 0.0445 <sup>§</sup>
	all data	R <sub>1</sub> = 0.0151, wR <sub>2</sub> = 0.0445
Weighting scheme	$w = 1/[\sigma^2(F_o^2) + (0.0107P)^2 + 1.6765P]$ where $P = (F_o^2 + 2F_c^2)/3$	
Extinction coefficient	0.1180(50)	
Largest diff. peak and hole	1.094 and -1.010 eÅ <sup>-3</sup>	
R.M.S. deviation from mean	0.169 eÅ <sup>-3</sup>	

<sup>£</sup> F is the structure factor and is proportional to the square root of the intensity of reflections; <sup>£</sup> F<sub>oo</sub> and F<sub>oc</sub> are the observed and calculated structure factors, respectively; <sup>§</sup> R<sub>1</sub> is Residual Factor, and wR<sub>2</sub> is weighted Residual factor. Here, R.M.S is abbreviation for Root Mean Square.

**Table 3** Atomic coordinates and equivalent isotropic and anisotropic atomic displacement parameter (Å<sup>2</sup>)

Label	Wyckoff Positions	x/a	y/b	z/c	U(eq)*
Ce01	2d	0.666667	0.333333	0.75001(8)	0.00225(18)
Cl02	6g	0.91360(13)	0.30105(14)	0.2501(2)	0.0033(2)

\* U(eq) is defined as one-third of the trace of the orthogonalized U<sub>ij</sub> tensor.

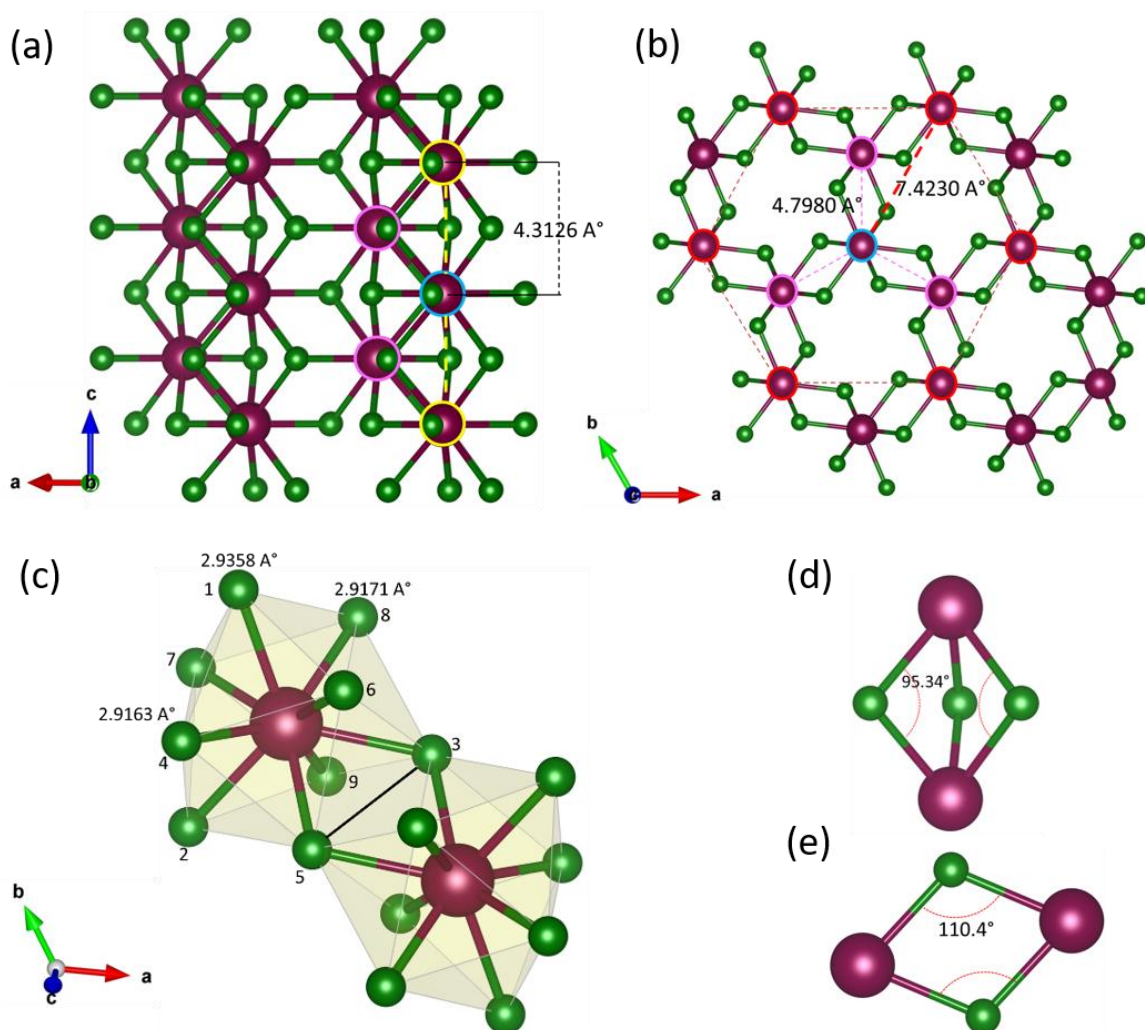


**Fig. 3.** Crystal structure of  $\text{CeCl}_3$  obtained using VESTA [16]. The brown balls represent Ce and smaller green balls represent Cl. (a) View along the  $b$ -axis ( $ac$ -plane) indicating nearest neighbor in yellow circles; (b) View along the  $c$ -axis ( $ab$ -plane) indicating second nearest neighbor in magenta and 3<sup>rd</sup> nearest neighbors in red; (c) 9-fold co-ordination of  $\text{Ce}^{3+}$  ions where Cl<sup>-</sup> ions numbered 1, 2 and 3 are coplanar with the central  $\text{Ce}^{3+}$  ion. The Cl<sup>-</sup> ions numbered 4-6 lie in a plane above and 7-9 in a plane below the plane formed by 1-3. These planes are perpendicular to a  $c$ -axis; (d) Ce-Cl-Ce nearest neighbor exchange pathways via  $95.4^\circ$  angle; (e) second nearest neighbor exchange pathway via  $110.4^\circ$  angle.

### 3.3 Raman Spectroscopy

Fig. 4 show the Raman spectra of a high-quality single crystal of  $\text{CeCl}_3$ . The observed spectra could be satisfactorily fitted using five Lorentzian line shape. For simplicity, the modes are labelled from  $R_1$  to  $R_5$  and their positions are:  $106.8 \text{ cm}^{-1}$ ,  $181.2 \text{ cm}^{-1}$ ,  $189 \text{ cm}^{-1}$ ,  $213 \text{ cm}^{-1}$ , and  $219.7 \text{ cm}^{-1}$ . In an older study,  $\text{CeCl}_3$  is reported to show six Raman modes at  $E_{2g}$  ( $106 \text{ cm}^{-1}$ ),  $A_g$  ( $176 \text{ cm}^{-1}$ ),  $E_{2g}$  ( $180 \text{ cm}^{-1}$ ),  $E_{1g}$  ( $193 \text{ cm}^{-1}$ ),  $A_g$  ( $216 \text{ cm}^{-1}$ ), and  $E_{2g}$  ( $218 \text{ cm}^{-1}$ ) [17]. The

comparison with our data suggests the presence of an extra peak at  $176\text{ cm}^{-1}$  in the spectra reported in Ref. [13]. Incidentally, in the isostructural  $\text{LaCl}_3$  only five Raman modes at  $108\text{ cm}^{-1}$ ,  $179\text{ cm}^{-1}$ ,  $186\text{ cm}^{-1}$ ,  $210\text{ cm}^{-1}$ , and  $217\text{ cm}^{-1}$  [18]. The possible reason for the extra mode in  $\text{CeCl}_3$  in Ref. [13] could be presence of local defects or impurities. Although previously reported study [17] had discussed the polarization dependence of a Raman active mode centered at  $179\text{ cm}^{-1}$ , a more careful polarization dependent analysis is still lacking to understand the symmetry ( $A_g$  or  $E_g$ ) of all the modes present in  $\text{CeCl}_3$ . Also, a temperature dependent study is needed to understand the evolution of Raman modes with temperature. The degenerate  $E_{1g}$  and  $E_{2g}$  Raman modes are expected to split under magnetic field into left- and right-handed circular polarization leading to a chiral behavior [23].

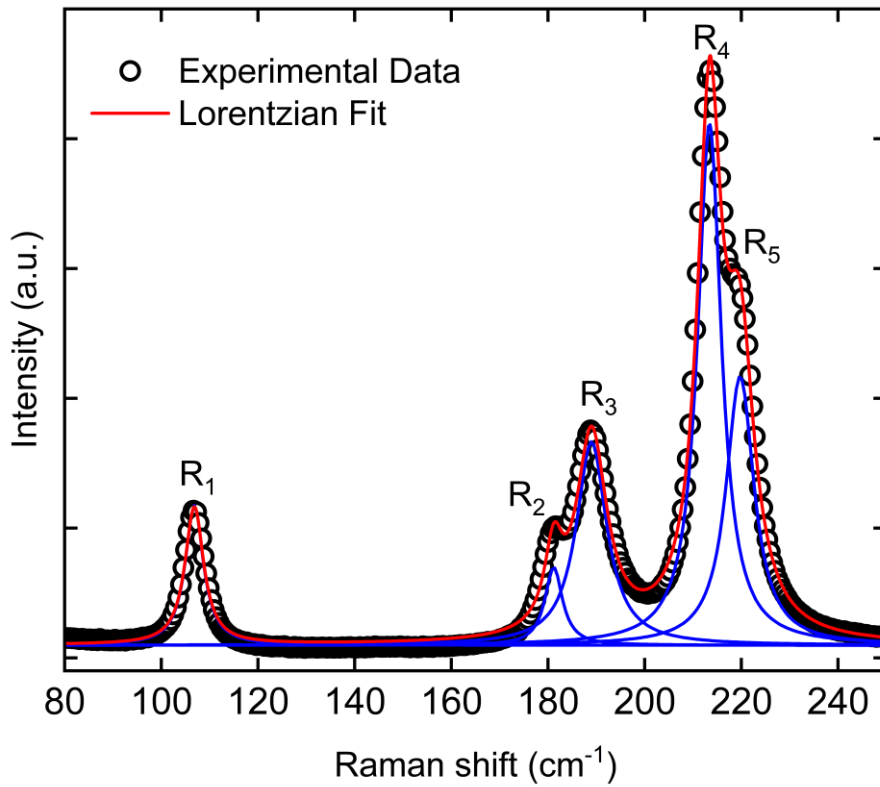


**Fig. 4.** The Raman spectra of  $\text{CeCl}_3$ . The five Raman modes are labelled  $R_1, R_2, \dots, R_5$ . The blue curves are individual Lorentzian fits for each mode. The red line through the data point is a total fitted spectrum obtained by adding up the individual Lorentzian. The raw data up to  $550\text{ cm}^{-1}$  is shown as Fig. S1 in the Supplementary Material.

### 3.4 Magnetic susceptibility

The low temperature magnetic Susceptibility ( $\chi$ ) of  $\text{CeCl}_3$  is shown in Fig. 5. The magnetic field was applied along the  $a$ -axis (i.e., perpendicular to the trigonal  $c$ -axis). Since the ordering

temperature of  $\text{CeCl}_3$  is below 2 K, we expect to see a paramagnetic behavior over the whole temperature range of our measurement from 4 K to 300 K. However, upon cooling,  $\chi(T)$  shows a broad peak at 50 K, followed by a sharp rise down below 25 K. A peculiar ZFC-FC splitting can also be seen. It is small, it appears well above the peak temperature, and it closes at low temperatures, i.e., the two branches approach each other with  $\chi_{\text{ZFC}} = \chi_{\text{FC}}$  at the 4 K. The reason for splitting is not clear at present. The average Ce-Ce interaction estimated from the Curie-Weiss analysis (*vide infra*) is too weak to explain the maxima near 50 K or the small thermomagnetic irreversibility around it. Further, the nearest neighbor ( $nn$ ) exchange ( $J_{nn}$ ) in  $\text{CeCl}_3$  is along the  $c$ -axis, and the  $nnn$  interaction ( $J_{nnn}$ ) is in the plane perpendicular to  $c$ -axis; the Ce-Cl-Ce bond angle ( $95^\circ$  versus  $110^\circ$ ) and Ce-Ce bond distances ( $4.3 \text{ \AA}$  versus  $4.7 \text{ \AA}$ ) are also comparable for the  $nn$  and  $nnn$  Ce ions. Thus, one-dimensionality in  $\text{CeCl}_3$  can be ruled out (the 1D chains show a maximum in  $\chi$  at a temperature close to  $J/2$  where  $J$  is the intrachain exchange coupling). A more plausible reason is that this peak arises due to the crystal field effect. The crystal field of trigonal symmetry will split the lowest  $J = 5/2$  manifold of  $\text{Ce}^{3+}$  into three Kramer's doublets located near 55 K and 155 K, as we shall see later from the analysis the magnetic specific heat. The other manifestation of crystal field splitting is the highly inflated values of Weiss temperature ( $\theta_{\text{CW}}$ ) and effective magnetic moment on  $\mu_{\text{eff}}$  from the high temperature Curie-Weiss fit: -158 K and  $4 \mu_{\text{B}}$ , respectively. This has to do with the fact that in derivation of Curie-Weiss law, we assume the splitting between the levels that contribute to the susceptibility to be very small compared to the scale  $k_{\text{B}}T$  of the temperature range over which the fit is performed. Such will be the case when the sample is cooled to sufficiently low temperature such that the contribution of the higher lying doublets is quenched and only the lowest Kramer's doublet contributes to the susceptibility. In the case of  $\text{CeCl}_3$  where the first excited doublet is located around 55 K, well below this temperature one should start seeing the contribution of the Zeeman split ground doublet. Indeed, below 25 K, there is an upturn which can be fitted to the Curie-Weiss law to get the moment associated with the lowest doublet and effective Ce-Ce interaction. We fitted the susceptibility data below 10 K using the modified Curie-Weiss equation:  $\chi = \chi_0 + \frac{C}{(T - \theta_{\text{CW}})}$ . The fitting is shown in the inset of Fig. 5. The best fit yields  $\chi_0 = 5.15 \times 10^{-4} \text{ emu/mol}$ ,  $\theta_{\text{CW}} = 0.2 \text{ K}$  and  $\mu_{\text{eff}} = 0.5 \mu_{\text{B}}$ . The electron spin resonance (ESR) of a  $\text{CeCl}_3$  crystal specimen by Hutchison et. al. [19] reported experimental  $g$  values as:  $g_{\parallel} \simeq 4.0366$  and  $g_{\perp} \simeq 0.17$  with respect to the  $c$ -axis. Hence, by using:  $\mu_{\text{eff}} = g \sqrt{J(J+1)}$  where

$g_{\perp}$  is 0.17, we obtained  $J \simeq \frac{5}{2}$ . This suggests that the ground state of  $\text{Ce}^{3+}$  in  $\text{CeCl}_3$  is a Kramer's doublet  $\pm \frac{5}{2}$  which is in agreement to the previously reported literature[9,11,19–21]

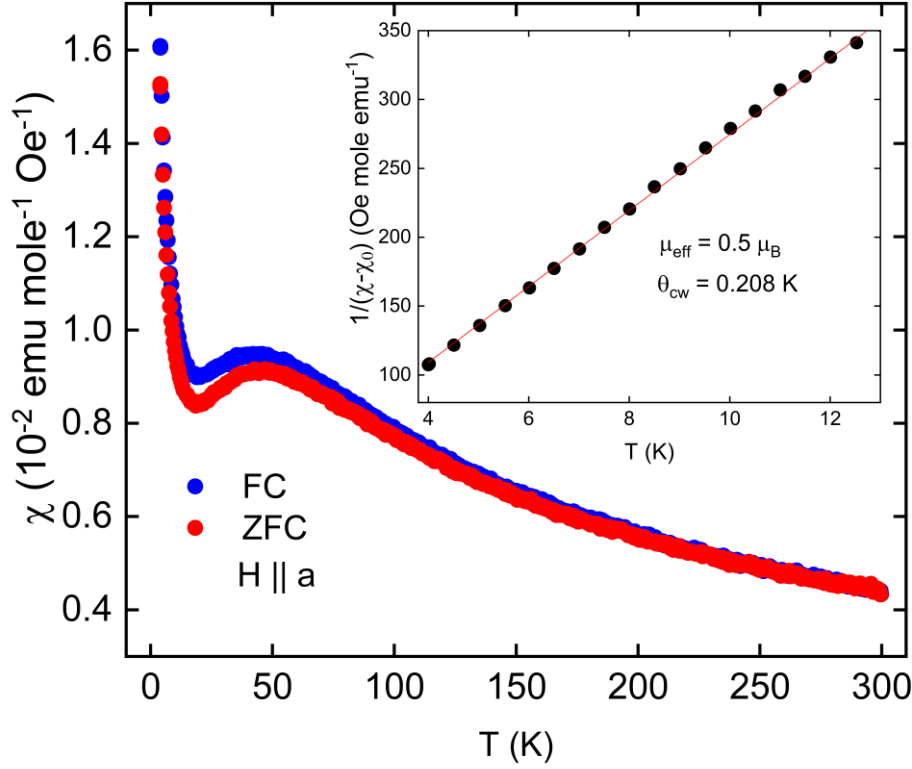


**Fig. 5.** (a) The magnetic susceptibility  $\chi$  of a  $\text{CeCl}_3$  crystal for field applied ( $H = 1$  kOe) parallel to the  $a$ -axis. Inset shows  $(\chi - \chi_0)^{-1}$ . The solid line is the best fit using the modified Curie-Weiss law (see text for details).

### 3.5 Specific heat

The specific heats of  $\text{CeCl}_3$  and  $\text{LaCl}_3$ , the latter being the non-magnetic analogue of  $\text{CeCl}_3$ , are measured between 250 K and 2 K as shown in Fig. 6a. The low-temperature data for  $\text{LaCl}_3$  can be fitted using the equation,  $C_p = \gamma T + \beta T^3$ , where  $\gamma$  and  $\beta$  corresponds to electronic and lattice contributions, respectively.  $\text{LaCl}_3$  being an insulator with an electronic band gap of 5.1 eV[8], the first term can be ignored. The data are replotted as  $C_p/T$  vs  $T^2$ . The variation appears linear (inset in Fig. 6a). Performing a linear-fit yield:  $\beta = \text{slope} = 5.68 \times 10^{-4} \text{ J mol}^{-1} \text{ K}^{-4}$ . From the obtained value of  $\beta$ , we calculated the Debye temperature  $\Theta_D = 239 \text{ K}$  using the formula  $\beta = 12\pi^4 N R / 5 \Theta_D^3$  where  $R$  is the universal gas constant. Note that this value of  $\Theta_D$  is not the

same as reported by Landau et. al. ( $\Theta_D = 155$  K) [9] . After checking their data, we found that the value to obtained is ignores the factor  $N$  (number of atoms per formula unit). Upon heating, the specific heat rises attaining the Dulong-Petit value of  $3NR$  ( $\approx 100 \text{ J mol}^{-1} \text{ K}^{-1}$ ) where  $N = 4$  is number of atoms per formula unit. In order to extract the 4f contribution to the specific heat, we subtracted the lattice part assuming  $\text{LaCl}_3$  to be the lattice template. Being isostructural to  $\text{CeCl}_3$  and having a comparable molecular weight,  $\text{LaCl}_3$  is a closest material to model the lattice specific heat of  $\text{CeCl}_3$ . Fig. 6b shows the 4f electrons contribution obtained by subtracting specific heat of  $\text{LaCl}_3$  from that of  $\text{CeCl}_3$ . The upturn below 2 K is due to the short-range ordering of  $\text{Ce}^{3+}$  ions and the broad peak centered around 30 K is attributed to the Schottky anomaly due to the crystal field splitting of the  $J = 5/2$  multiplet into three Kramer's doublets. The subtracted specific heat contribution, due the 4f electrons can be fitted using the three-level Schottky expression, given below:

$$C_{\text{Schottky}} = R \frac{1}{T^2} \left\{ \frac{(g_1 g_0 \Delta_1^2 e^{-\beta \Delta_1} + g_2 g_0 \Delta_2^2 e^{-\beta \Delta_2})}{(g_0 + g_1 e^{-\beta \Delta_1} + g_2 e^{-\beta \Delta_2})} + \frac{(g_1 g_2 e^{-\beta(\Delta_1 + \Delta_2)})[\Delta_1(\Delta_1 - \Delta_2) + \Delta_2(\Delta_2 - \Delta_1)]}{(g_0 + g_1 e^{-\beta \Delta_1} + g_2 e^{-\beta \Delta_2})} \right\},$$

where  $\Delta_1$  and  $\Delta_2$  is the energy of the first and second excited doublets above the ground state,  $g_0 = g_1 = g_2 = 2$  is the degeneracy of three doublets [22]. The best fit to the experimental data is obtained for  $\Delta_1 = 55$  K and  $\Delta_2 = 155$  K in good agreement with previous reports where the position of level was reported at 59 K from the magnetic specific heat between 3.5 K and 4.2 K [9]. The attempts to fit the broad peak using a two-level Schottky where only ground and first excited state doublet is considered does not give a satisfactory fit to the experimental data (see Fig. S2 in the Supplementary Material).

Coming now to the field dependence of low-temperature specific heat of our  $\text{CeCl}_3$  crystal. The magnetic field dependent measurements are summarized in Fig. 6b. The in-field measurements ( $H \parallel a$ ) are superimposed with the data from a previous study [6] where specific heat is reported below 4.2 K up to an applied magnetic field of 14 kOe. Our zero-field data overlaps nicely with the zero-field data in Ref. [9]. In zero-field,  $C_p$  in our data shows a weak upturn below 4 K, which is precursory to the long-range ordering of the Ce moments at low temperatures as is evident from the presence of a sharp peak near in  $C_p$  near 110 mK (data plotted from Ref. [9]), which indicates long-range ordering. The entropy below 2 K ( $\sim R \ln 2$ ) corroborates the long-range ordering (*vide infra*). Due to weak exchange coupling between the Ce moments, even a weak applied magnetic field has a strong effect on the specific heat peak, which broadens and shifts toward higher temperatures as the field increases, occurring near 2.5 K in an applied magnetic field of 30 kOe.

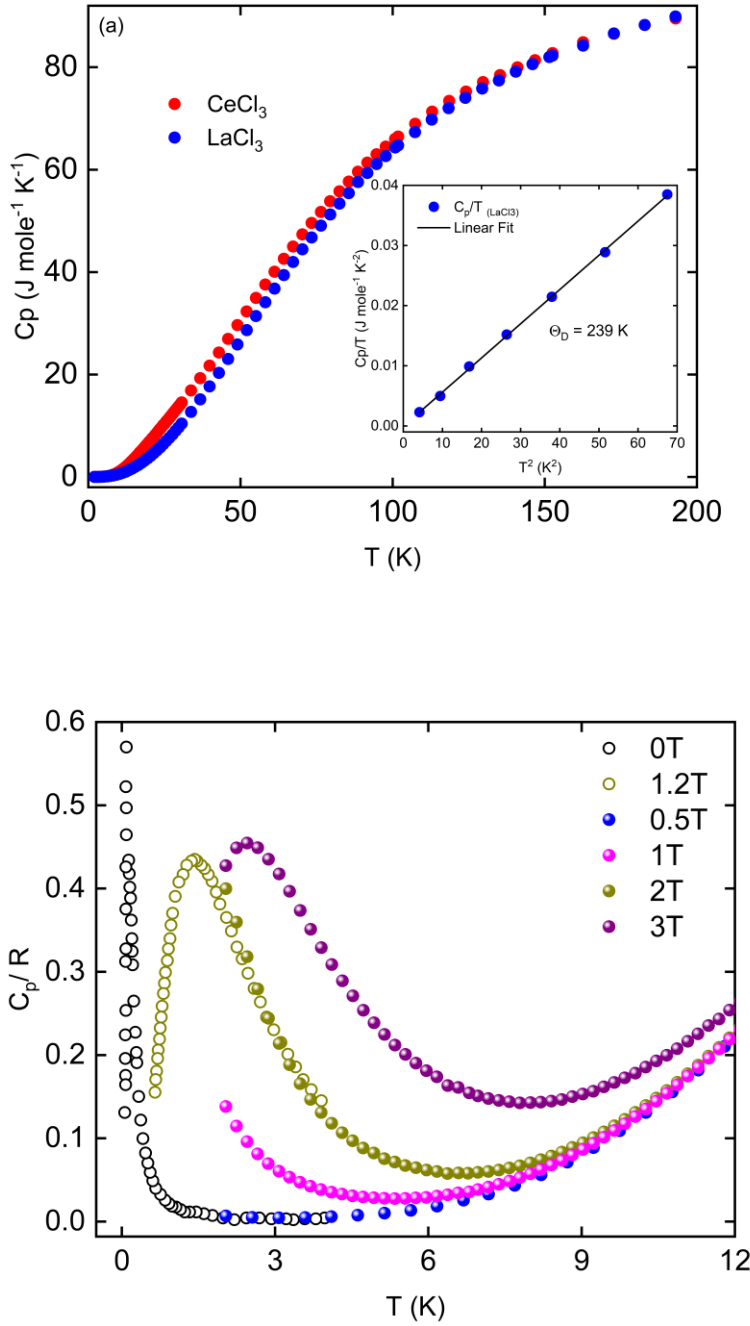


**Fig. 6.** (a) Temperature variation of the specific heat of  $\text{CeCl}_3$  (red circle) and  $\text{LaCl}_3$  (blue circle) in the temperature range of 200 K down to 2 K. The inset show the  $C_p/T$  vs  $T^2$  plot for  $\text{LaCl}_3$ . The Debye temperature estimated from the coefficient of the  $T^3$  term is also shown. (b) Variation of  $C_p$  with temperature under different applied magnetic fields. The closed circles are the experimental data from this work and open circle are data points taken from Landau *et al.* [9].

Unfortunately, our attempts to measure the specific heat at higher field turned unsuccessful as the crystal shattered into pieces upon cooling below 4.5 K under a field of 50 kOe. This is due to the strong magnetic torque that acts on the specimen due to highly ordered Ce moments in the lower of the two Zeeman split  $\pm 5/2$  levels (i.e., Ce moments preferably occupying the

lower Zeeman state even at temperatures as high as  $\sim 4.5$  K due to a relatively large Zeeman splitting compared to the splitting due to the exchange field alone). A slight discrepancy between the in-field data in our study and data from Ref. [9] (12 kOe data from Ref. [9] is close to our 20 kOe, indicating a small field off-set), may arise from the difference in the field orientation.

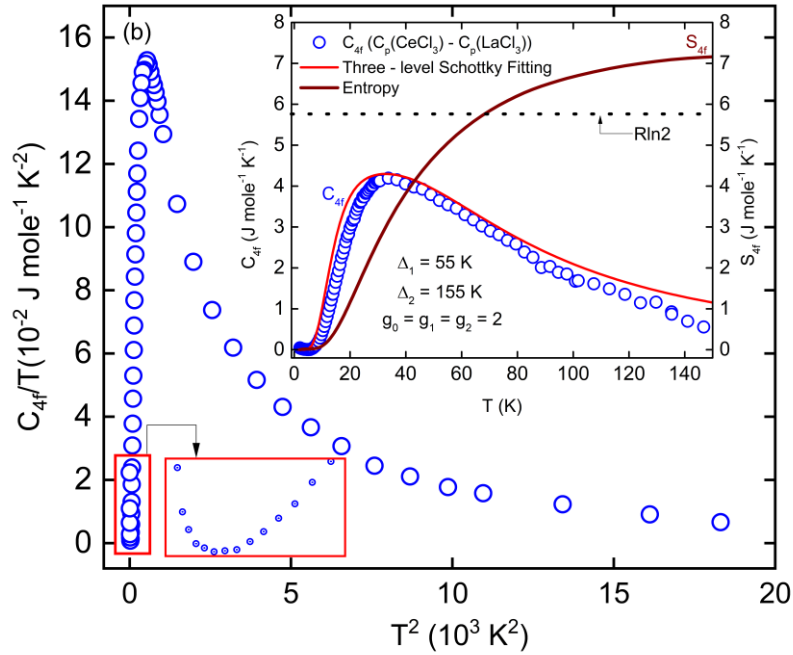


**Fig. 7.** The temperature variation of magnetic specific heat ( $C_{4f}$ ) shown as  $C_{4f}/T$  versus  $T^2$  in the main panel. The inset shows  $C_{4f}$  (blue circle). The red line is the best fitted to the data using the three-level Schottky model (see text for details). The right vertical axis in the inset shows the variation of  $S_{4f}$  with temperature. The  $S_{4f}$  with low-temperature data included in the literature is shown Fig. S3 in the Supplementary Material.

We estimated the entropy associated with the 4f electrons,  $S_{4f}$ , above  $T_0 = 2$  K, using the formula:  $S_{4f} = \int_{T_0}^{T_1} C_{4f}/T' dT'$ . As shown in the inset of Fig. 7, the entropy exceeds the  $R\ln 2$  value near 70 K and continues to rise up to the highest temperature in our measurements. This behavior needs a comment: first, we have not considered a large chunk of  $S_{4f}$  below 2 K, the range over which the Ce moments order magnetically. If we do this by including the specific heat data from previous literature [9] where data are reported between 0.05 K and 4 K and by smoothly extrapolating this data further down to 0, the resulting  $S_{4f}$  plot plateau at  $R\ln 2$  and the width of this plateau extends from  $T < 1$  K and 10 K. The attainment of  $R\ln 2$  at low temperatures is due to the long-range ordering of the Ce moments (See Supplementary Material). The excited states contribute to  $S_{4f}$  only above 10 K, the temperature above which



$C_{4f}$  in Fig. 7 rises sharply. As shown in the Supplementary Material Fig. S3,  $S_{4f}$  overshoots the value  $R_{ln4}$  near 70 K. Thus,  $S_{4f}$  crossing  $R_{ln2}$  near 70 K in Fig. 7 in the main text is the contribution sans the  $R_{ln2}$  contribution from the ground state doublet.

#### 4 Summary and conclusions

High-quality single crystals of  $CeCl_3$  are grown using the Bridgman-Stockbarger method in an infrared image furnace. At first attempts to grown crystals using static Bridgman method were also tried. Using both methods, mm-sized single crystals were obtained with the difference that crystals obtained using the Bridgman-Stockbarger method were bigger in size, fully transparent and higher in yield compared to the crystals obtained using the static Bridgman technique. The grown crystals were characterized using single-crystal x-ray diffraction, x-ray diffraction in Bragg Brentano geometry, x-ray Laue diffraction. We show that  $CeCl_3$  crystallizes in a trigonal crystal structure with space group  $P\bar{3}$  (No. 147). The composition measured using an EDX probe attached to the FESEM showed that the grown crystals have the required  $Ce : Cl \equiv 1 : 3$  composition. The crystals are highly sensitive to moisture and react with it within minutes to form white powder (oxychlorides). The low-temperature thermal and magnetic properties of the grown crystals are studied between 2 K and 300 K. The magnetic susceptibility shows a broad peak centered around 50 K. This has been argued to arise from the crystal field splitting of  $J = 5/2$  multiplet into three Kramer's doublets. Below 25 K, the susceptibility shows a steep increase upon cooling. The low temperature ( $T < 10$  K) susceptibility when fitted using the modified Curie-Weiss law yields a Curie-Weiss temperature of 0.2 K suggesting that the Ce spins are very weakly exchanged coupled. The effective magnetic moment confirms that the crystal field split ground state of  $Ce^{3+}$  is  $|5/2, \pm 5/2\rangle$ . The specific heat data obtained in the temperature range of 2 K to 300 K do not show any sharp anomalies, but a weak upturn is observed at low temperatures ( $T < 4$  K) which is attributed to the short-range correlations between the Ce spins. The analysis of the 4f specific heat suggests that the first and second excited Kramer's doublet are situated around 55 K and 155 K. Since, the  $nn$  and  $nnn$  exchange interactions are of comparable magnitude, the bond angles Ce-Cl-Ce and bond distances Ce-Ce being of comparable values for the two exchange pathways, further investigations using neutron scattering and muon spin relaxation techniques would be useful in capturing the exact magnetic ground state and excitations of  $CeCl_3$ . Raman spectroscopy of  $CeCl_3$  showed five Raman active modes at modes at  $106.8\text{ cm}^{-1}$ ,  $181.2\text{ cm}^{-1}$ ,  $189\text{ cm}^{-1}$ ,  $213\text{ cm}^{-1}$ , and  $219.7\text{ cm}^{-1}$ . In future, polarization, temperature, and magnetic field dependent Raman spectroscopy are

needed to completely understand the evolution of Raman modes and the correlation between the spin and lattice degrees of freedom. The degenerate infrared active  $E_{1u}$  phonon mode will be interesting to study in future as the electric dipole moment associated with this phonon can be resonantly excited by the electric field of the applied laser pulse. This can yield large vibrational amplitudes that can act on the spins through the inverse spin-phonon coupling as predicted in a recent theoretical work [11].

## References

- [1] L. Balents, Spin liquids in frustrated magnets, *Nature*. 464 (2010) 199–208.  
<https://doi.org/10.1038/nature08917>.
- [2] S. Widmann, V. Tsurkan, D.A. Prishchenko, V.G. Mazurenko, A.A. Tsirlin, A. Loidl, Thermodynamic evidence of fractionalized excitations in  $\alpha$ -RuCl<sub>3</sub>, *Phys. Rev. B*. 99 (2019) 094415. <https://doi.org/10.1103/PhysRevB.99.094415>.
- [3] J. Chaloupka, G. Khaliullin, Magnetic anisotropy in the Kitaev model systems Na<sub>2</sub>IrO<sub>3</sub> and RuCl<sub>3</sub>, *Phys. Rev. B*. 94 (2016) 064435. <https://doi.org/10.1103/PhysRevB.94.064435>.
- [4] J. Xing, E. Feng, Y. Liu, E. Emmanouilidou, C. Hu, J. Liu, D. Graf, A.P. Ramirez, G. Chen, H. Cao, N. Ni, Néel-type antiferromagnetic order and magnetic field-temperature phase diagram in the spin-12 rare-earth honeycomb compound YbCl<sub>3</sub>, *Phys. Rev. B*. 102 (2020) 014427. <https://doi.org/10.1103/PhysRevB.102.014427>.
- [5] W.H. Zachariasen, Crystal chemical studies of the 5f-series of elements. I. New structure types, *Acta Crystallogr.* 1 (1948) 265–268. <https://doi.org/10.1107/s0365110x48000703>.
- [6] B. Morosin, Crystal Structures of Anhydrous Rare-Earth Chlorides, *J. Chem. Phys.* 49 (1968) 3007–3012. <https://doi.org/10.1063/1.1670543>.
- [7] D.H. Templeton, C.H. Dauben, Lattice Parameters of Some Rare Earth Compounds and a Set of Crystal Radii, *J. Am. Chem. Soc.* 76 (1954) 5237–5239. <https://doi.org/10.1021/ja01649a087>.
- [8] K.-H. Park, S.-J. Oh, Electron-spectroscopy study of rare-earth trihalides, *Phys. Rev. B*. 48 (1993) 14833–14842. <https://doi.org/10.1103/PhysRevB.48.14833>.
- [9] D.P. Landau, J.C. Doran, B.E. Keen, Thermal and magnetic properties of CeCl<sub>3</sub>, *Phys. Rev. B*. 7 (1973) 4961–4979. <https://doi.org/10.1103/PhysRevB.7.4961>.
- [10] J.H. Colwell, B.W. Mangum, D.B. Utton, Low-temperature magnetic properties of some hexagonal rare-earth trihalides, *Phys. Rev.* 181 (1969) 842–854.

<https://doi.org/10.1103/PhysRev.181.842>.

- [11] D.M. Juraschek, T. Neuman, P. Narang, Giant effective magnetic fields from optically driven chiral phonons in 4f paramagnets, *Phys. Rev. Res.* 4 (2022) 013129. <https://doi.org/10.1103/PhysRevResearch.4.013129>.
- [12] H.Gunsilius, Darstellung von Selten- Erd-Trichloriden uber chemischen Transport mit Aluminiumtrichlorid H. GUNSILIUS~), W., 650 (1987) 35–40.
- [13] S. Mroczkowski, Preparation of single crystals of  $\text{EuCl}_3$  and related polyvalent halides, *J. Cryst. Growth.* 6 (1970) 147–150. [https://doi.org/10.1016/0022-0248\(70\)90033-3](https://doi.org/10.1016/0022-0248(70)90033-3).
- [14] M. Voda, M. Al-Saleh, G. Lobera, R. Balda, J. Fernández, Crystal growth of rare-earth-doped ternary potassium lead chloride single crystals by the Bridgman method, *Opt. Mater. (Amst).* 26 (2004) 359–363. <https://doi.org/10.1016/j.optmat.2003.12.019>.
- [15] N. Pistawala, D. Rout, K. Saurabh, R. Bag, K. Karmakar, L. Harnagea, S. Singh, Crystal growth of quantum materials: a review of selective materials and techniques, *Bull. Mater. Sci.* 45 (2021) 10. <https://doi.org/10.1007/s12034-021-02612-1>.
- [16] K. Momma, F. Izumi, VESTA 3 for three-dimensional visualization of crystal, volumetric and morphology data, *J. Appl. Crystallogr.* 44 (2011) 1272–1276. <https://doi.org/10.1107/S0021889811038970>.
- [17] T.C. Damen, A. Kiel, S.P.S. Porto, S. Singh, The Raman effects of  $\text{CeCl}_3$  and  $\text{PrCl}_3$ , *Solid State Commun.* 6 (1968) 671–673. [https://doi.org/10.1016/0038-1098\(68\)90191-9](https://doi.org/10.1016/0038-1098(68)90191-9).
- [18] F.T. Hougen, S. Singh, No Title, *Proc. R. Soc. A* 227 (1964) 193.
- [19] C.A. Hutchison, E. Wong, Paramagnetic resonance in rare earth trichlorides, *J. Chem. Phys.* 29 (1958) 754–760. <https://doi.org/10.1063/1.1744587>.
- [20] B. Schneider, Magnetische Eigenschaften von wasserfreiem Cer- und Praseodymchlorid, *Zeitschrift Für Phys.* 177 (1964) 179–189. <https://doi.org/10.1007/BF01375336>.
- [21] P. Thalmeier, P. Fulde, Optical phonons of Rare-Earth halides in a magnetic field, *Zeitschrift Für Phys. B Condens. Matter.* 26 (1977) 323–328. <https://doi.org/10.1007/BF01570742>.
- [22] M. de Souza, R. Paupitz, A. Seridonio, R.E. Lagos, Specific Heat Anomalies in Solids Described by a Multilevel Model, *Brazilian J. Phys.* 46 (2016) 206–212. <https://doi.org/10.1007/s13538-016-0404-9>.

- [23] G. Schaack, Magnetic field dependent splitting of doubly degenerate phonon states in anhydrous cerium-trichloride, *Zeitschrift Für Phys. B Condens. Matter.* 26 (1977) 49–58.  
<https://doi.org/10.1007/BF01313371>.
- [24] Bruker APEX3, Analytical X-ray Instruments Inc., Madison, Wisconsin, USA, 2016.
- [25] Bruker SAINT, Analytical X-ray Instruments Inc., Madison, Wisconsin, USA, 2016.

**Figure captions:**

**Fig. 1.** (a) Crystal growth of  $\text{CeCl}_3$  using a four-mirror image furnace equipped with 1 kW halogen lamps. The lower part below the solid-liquid interface is the  $\text{CeCl}_3$  crystal being grown. (b) Images of the crystals pieces obtained after cutting the crystal boule shown in the inset.

**Fig. 2.** (a) The x-ray diffraction pattern carried out in the Bragg-Brentano geometry on the specimen shown in the inset on the right. The left inset shows the Laue diffraction pattern from a similar specimen as shown here.

**Fig. 3.** Crystal structure of  $\text{CeCl}_3$  obtained using VESTA [16]. The brown balls represent Ce and smaller green balls represent Cl. (a) View along the  $b$ -axis ( $ac$ -plane) indicating nearest neighbor in yellow circles; (b) View along the  $c$ -axis ( $ab$ -plane) indicating second nearest neighbor in magenta and third nearest neighbors in red; (c) 9-fold co-ordination of  $\text{Ce}^{3+}$  ions where  $\text{Cl}^-$  ions numbered 1, 2 and 3 are coplanar with the central  $\text{Ce}^{3+}$  ion. The  $\text{Cl}^-$  ions numbered 4-6 lie in a plane above and 7-9 in a plane below the plane formed by 1-3. These planes are perpendicular to a  $c$ -axis; (d) Ce-Cl-Ce nearest neighbor exchange pathways via  $95.4^\circ$  angle; (e) second nearest neighbor exchange pathway via  $110.4^\circ$  angle.

**Fig. 4.** The Raman spectra of  $\text{CeCl}_3$ . The five Raman modes are labelled  $R_1, R_2, \dots, R_5$ . The blue curves are individual Lorentzian fits for each mode. The red line through the data point is a total fitted spectrum obtained by adding up the individual Lorentzian. The raw data up to  $550 \text{ cm}^{-1}$  is shown in Fig. S1 in the Supplementary Material.

**Fig. 5.** (a) The magnetic susceptibility  $\chi$  of a  $\text{CeCl}_3$  crystal for field applied ( $H = 1 \text{ kOe}$ ) parallel to the  $a$ -axis. Inset shows  $(\chi - \chi_0)^{-1}$ . The solid line is the best fit using the modified Curie-Weiss law (see text for details).

**Fig. 6.** (a) Temperature variation of the specific heat of  $\text{CeCl}_3$  (red) and  $\text{LaCl}_3$  (blue) in the temperature range of 200 K down to 2 K. The inset show the  $C_p/T$  vs  $T^2$  plot for  $\text{LaCl}_3$ . The Debye temperature estimated from the coefficient of the  $T^3$  term is also shown. (b) Variation of  $C_p$  with temperature under different applied magnetic fields. The closed circles are the experimental data from this work and open circle are data points taken from Landau *et al.* [9].

**Fig. 7.** The temperature variation of magnetic specific heat ( $C_{4f}$ ) shown as  $C_{4f}/T$  versus  $T^2$  in the main panel. The inset shows  $C_{4f}$  (blue circle). The red line is the best fitted to the data using

the three-level Schottky model (see text for details). The right vertical axis in the inset shows the variation of  $S_{4f}$  with temperature. The  $S_{4f}$  with low-temperature data included in the literature is shown in Fig. S3 in the Supplementary Material.